Tenth International Conference on Computational Fluid Dynamics (ICCFD10), Barcelona,Spain, July 9-13, 2018

ICCFD10-2018-321

An Actuator Line Model Simulation of two semi-aligned wind turbine models, operating above-rated wind speed

A. Guggeri*, M. Draper*, G. Usera* and F. Campagnolo**
Corresponding author: aguggeri@fing.edu.uy

* Facultad de Ingeniería, Universidad de la República,
Julio Herrera y Ressig 565, Montevideo, Uruguay.
** Wind Energy Institute, Technische Universität München,
Boltzmannstraße 15, D-85748 Garching bei München, Germany.

Abstract: Wind energy is expanding rapidly worldwide, being horizontal axis wind turbines (HAWT) the technology of greater installed capacity. A characteristic of this technology is the need to limit the production of power when the wind speed is greater than the rated one. In this work we show results of a validated numerical method applied to the simulation of two model wind turbines operating at above rated wind speed, showing their ability to control the power output. Five different wind velocity profiles at the inlet of the simulations domain were considered. The results of one simulation are compared to data obtained from a well known wind tunnel campaign, finding good agreement between the temporal evolution of the involved variables.

Keywords: Actuator Line Model, LES, Wind Turbines, Power Control.

1 Introduction

In the last decades wind energy has had a very large expansion, being horizontal axis wind turbines (HAWT) the technology of greater installed capacity among renewable energies [1]. Due to the transient nature of the wind flow through a wind farm, the state-of-the-art methodology to simulate it consists of Large Eddy Simulations (LES), while two approaches exist in order to represent the presence of a wind turbine in a simulation: actuator models, in which the blades are represented as body forces, and direct representation of the blade's geometry through the computational mesh. Among the actuator models, the Actuator Line (AL) has been widely validated, taking into account different inflow conditions, showing to reproduce with reasonable accuracy the wind flow in the wake of a wind turbine with moderately computation cost. Some validation cases and applications of this methodology can be seen in [2] [3] [4] [5] [6] [7] [8] [9] [10]. To compute the aerodynamic forces along the blades, as well as integral quantities such as total power and thrust, an aero-elastic code, such as FAST [11] or FLEX5 [12] can be coupled to the LES-AL framework.

A characteristic of a HAWT is its capacity to control the active power production, when the wind speed up-stream of the rotor is greater than the rated one. To accomplish this, the wind turbines regulate the torque imposed by the electric generator and the angle of the blades (pitch), in order to control the angular speed of the rotor, and thus the power output [13] [14]. These turbine controllers may be implemented in the aero-elastic code, for example: in [15] the FAST code was coupled with a LES solver and an actuator disk to investigate wake structures and interaction effects between dynamically controlled turbines; in [16] the CFD code developed by NREL, SOWFA [4], was coupled with FAST, with individual controllers for each turbine and also with a super-controller, which enables control at wind plant level; in [17] the 3D general purpose flow solver, EllipSys3D [9] and the Actuator Line method are combined with FLEX5, which supports control algorithms for the generator and the pitch systems, although the focus of that work is not dynamically controlling the wind turbines.

Another approach to simulate the aerodynamics and controllers of the wind turbines is to directly implement them in the CFD code, rather than coupling with the aero-elastic model. Examples of this are given at [18], where the generator torque controller was implemented in the LES-AL framework VWis (Virtual Wind Simulator), and in [19] where a modeling framework is proposed and validated, combining LES, the actuator-disk model and a turbine-model-specific relationship between shaft torque and rotational speed, to simulate turbine wakes and associated power losses in wind farms.

In this work we present simulations of the wind flow and the operation of wind turbines (WT) operating at wind speeds above the rated one. To simulate the wind flow the validated CFD solver caffa3d.MBRi [20][21] was used, and the wind turbines where represented by the AL. A closed-loop active power controller, based on the one described in [22], was implemented directly in caffa3d.MBRi by adding a series of subroutines. This controller enables the operation of wind turbines in the whole range of wind speeds. For validation, the simulation results were compared to data obtained from a well known wind tunnel experimental campaign performed by the Wind Energy Institute of Technische Universität München (TUM). These tests were conducted within the boundary layer wind tunnel of the Politecnico di Milano [23], where a scaled wind farm, composed of two wind turbine models already used within other research projects [24, 25, 26], has been employed.

This work is a complement of the paper [27] also presented in this conference, in which simulations of the same model wind turbines were performed with the same CFD code, but considering another arrangement of the turbines and different operational conditions to those presented in the current paper. The rest of this paper is organized as follows: in the next Section the numerical model is described; Section 3 presents the wind tunnel campaign, used for validation of the simulations. In Section 4 the numerical setup of the simulations and the results are presented. Finally conclusions and future work are proposed in Section 5.

2 Numerical Model

2.1 CFD solver

caffa3d.MBRi [21] [20] is an open source, finite volume (FV) code, second order accurate in space and time, parallelized with MPI, in which the domain is divided in unstructured blocks of structured grids. The mathematical model comprises the mass balance equation (1) and momentum balance equation (2) for a viscous incompressible fluid, together with generic passive scalar transport equation (3) for scalar field ϕ with diffusion coefficient Γ. Note that (2) has been written only for the first Cartesian direction $\hat{e}_1$. The balance equations are written for a region Ω, limited by a closed surface S, with outward pointing normal $\hat{n}_S$.

$$\int_S (\vec{v} \cdot \hat{n}_S)\, dS = 0 \tag{1}$$

$$\int_\Omega \rho \frac{\partial u}{\partial t} d\Omega + \int_S \rho u\, (\vec{v} \cdot \hat{n}_S)\, dS =$$

$$\int_\Omega \rho\beta\, (T - T_{ref})\, \vec{g} \cdot \hat{e}_1 d\Omega + \int_S -p\hat{n}_S \cdot \hat{e}_1 dS + \int_S (2\mu D \cdot \hat{n}_S) \cdot \hat{e}_1 dS \tag{2}$$

$$\int_\Omega \rho \frac{\partial \phi}{\partial t} d\Omega + \int_S \rho\phi\, (\vec{v} \cdot \hat{n}_S)\, dS = \int_S \Gamma\, (\nabla\phi \cdot \hat{n}_S)\, dS \tag{3}$$

where $\vec{v} = (u, v, w)$ is the fluid velocity, ρ is the density, β is the thermal expansion factor, T is the fluid temperature and T_{ref} a reference temperature, $\vec{g}$ is the gravity, p is the pressure, μ is the dynamic viscosity of the fluid and D is the strain tensor. The use of equations in their global balance form, together with the finite volume method, as opposed to the differential form, favors enforcing conservation properties for fundamental magnitudes as mass and momentum into the solving procedure [28].

To deal with the linearization and subsequent coupling of linear systems for each equation in the mathematical model, an outer-inner iteration scheme for each time step is employed, as shown in Figure 1. Linear systems for each equation in the mathematical model are sequentially assembled and undergo inner iterations with SIP or AMG-SIP linear solvers. The outer loop is repeated within each time step until the desired level of convergence is achieved before continuing to the next time step.

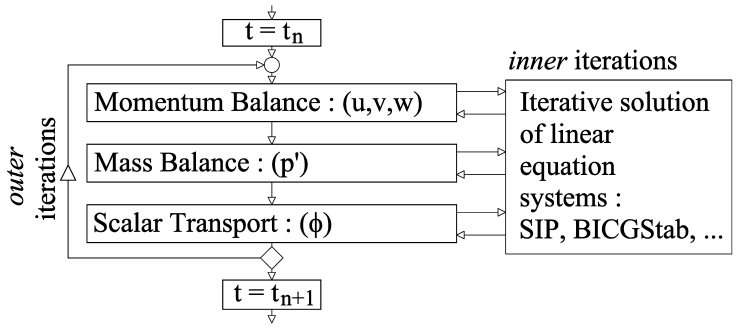

Figure 1: Iteration scheme for one time step (adapted from [28]).

Representation of complex geometries can be handled through a combination of body fitted grids and the immersed boundary method over both Cartesian and body fitted grid blocks. Geometrical properties and flow properties, which are expressed in primitive variables, are always expressed in a Cartesian coordinate system, using a collocated arrangement. Regarding the turbulence model, different subgrid scale models in the context of Large Eddy Simulation (LES) are implemented: the standard Smagorinsky model [29] with damping function for smooth [28] and rough surfaces [30], the dynamic Smagorinsky model [31] with different averaging schemes, the dynamic mixed Smagorinsky model [32] and the scale-dependent dynamic Smagorinsky model [33] with different averaging schemes. Further details of the solver together with validations can be found in [21, 20].

2.2 Actuator Line Model

The ALM has been implemented in the code [34] to represent wind turbines rotors in the simulations. Despite it is recommended to use a spatial resolution of at least R/30 and to set the time step size in order to limit the movement of the rotor tip to a grid cell length in each time step [14], the ALM has been evaluated with coarser resolutions [35] [34] [36] [37] [38] [39], still obtaining acceptable results.

Each blade is represented as a line that moves with the rotational speed of the rotor and it is discretized in radial sections where the aerodynamic forces are computed (Figure 2, left). The geometrical properties of the blades (chord length and twist angle (β) as well as aerodynamic properties (lift and drag coefficients) are necessary to compute the force in each radial section. The former are obtained directly from the model wind turbine, while the aerodynamic coefficients are computed from tabulated data of the corresponding airfoil. At each radial section the aerodynamic force is computed as

$$\vec{f} = -\frac{1}{2}\rho V_{rel}^2 c(C_L \vec{e_L} + C_D \vec{e_D})dr \tag{4}$$

where ρ is the air density, V_{rel} is the relative velocity, c is the chord length, C_L is the lift coefficient, C_D is the drag coefficient, $\vec{e_L}$ is a unit vector in the direction of the lift force, $\vec{e_D}$ is a unit vector in the direction of the drag force and dr is the length of the radial section (see Figure 2 , right). Prandtl's tip loss correction factor is applied, as it has shown to improve the results [35].

After computing the aerodynamic forces, it is required to project them onto the computational domain as a body force field. To accomplish this, a smearing Gaussian function is used, taking into account the distance between each grid cell and radial section,and three smearing parameters, one for each direction (n normal, r radial and t tangential).

$$f(d_n, d_r, d_t) = \frac{1}{\epsilon_n \epsilon_r \epsilon_t \pi^{1.5}} e^{-(\frac{d_n}{\epsilon_n})^2} e^{-(\frac{d_r}{\epsilon_r})^2} e^{-(\frac{d_t}{\epsilon_t})^2} \tag{5}$$

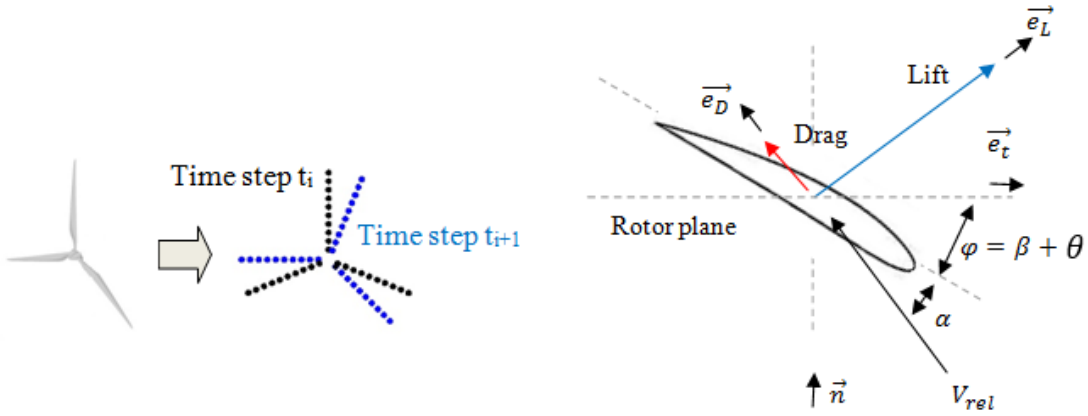

Figure 2: ALM rotor representation (left) and a cross-sectional airfoil radial section (right).

2.3 Power Control System

At each time step of the simulation, the resulting aerodynamic torque applied to the rotor shaft (M_{aero}) is computed by integration of the tangential forces along the blades, and the rotational speed is obtained from the rotor second cardinal equation (6), where M_{gen} is the generator torque, ω is the angular speed of the rotor at the current time step, I is the sum of the rotor, shaft and generator inertia considered at the low-speed side. Δt corresponds to the temporal step and ω_{t-1} accounts for the rotational speed of the previous time step. It is worth mentioning that in each external iteration (see Figure 1) the aerodynamic torque is computed and a different value may be obtained, so a different angular speed may also be obtained. On the other side, to compute the generator torque and update the position of the blades, the rotational speed is needed, but those quantities should be kept constant along the external iterations, as they belong to the same time step. To solve this issue, only the angular speed of the first external iteration is considered to compute the mentioned variables, then keeping their values constant for the rest of the externals iterations, regardless of the value the rotor speed might take in later iterations.

$$I\frac{d\omega}{dt} = M_{aero} - M_{gen} \Rightarrow \omega = \frac{(M_{aero} - M_{gen})}{I}\Delta t + \omega_{t-1} \tag{6}$$

Finally, the aerodynamic and electric power are calculated as the rotational speed multiplied by the shaft aerodynamic torque and the generator torque, respectively (equation 7).

$$\begin{aligned} P_{aero} &= M_{aero}.\omega \\ P_{electric} &= M_{gen}.\omega \end{aligned} \tag{7}$$

A basic characteristic of HAWTs is their ability to control the power output [22], when they are subject to the natural spacial and temporal variations of the wind speed flow, and as consequence to the variation of the forces acting on the rotor. The conventional approach to accomplish this is the design of two control systems which work independently, at the below-rated and above-rated wind-speed range. Respectively, these systems are the generator-torque controller, whose objective is to maximize power capture below the rated operation point, and the rotor-collective blade-pitch controller, with the goal of regulating the generator speed, and thus the rotor angular speed, at the rated operation point [13].

At the below-rated wind speed range, usually called Region 2, the generator torque is computed as a tabulated function, according to equation 8, where K is a constant that optimizes the power extraction from the wind and which depends on the aerodynamics and geometrical characteristics of the blades. The pitch-angle of the blades is fixed at its minimum value, in order to optimize the power extraction from the wind.

$$M_{gen} = K\omega^2 \tag{8}$$

At the above-rated wind-speed range, Region 3, M_{gen} is kept constant at its rated value. The rotor-collective blade-pitch-angle values are computed using a gain-scheduled proportional-integral (PI) control on the speed error ($\Delta\omega$) between the current WT speed and the rated speed (ω_{rated}). In equation 9, θ is the pitch angle (see Figure 2), K_I and K_P account for the proportional and integral gains respectively. The integral term accounts for the accumulated error over time, and in the simulations is computed by simply adding $\Delta\omega$ to its previous value, in each time step. The pitch-angle values and its rate of change are limited by saturation values. This PI controller ensures that ω fluctuates around its reference value, and so the active power output fluctuates around the active power rated value, P_{ref}. Figure 3 shows a flowchart of the control system that was implemented in the code.

$$\theta = K_P\Delta\omega + K_I\int_0^t \Delta\omega dt \tag{9}$$

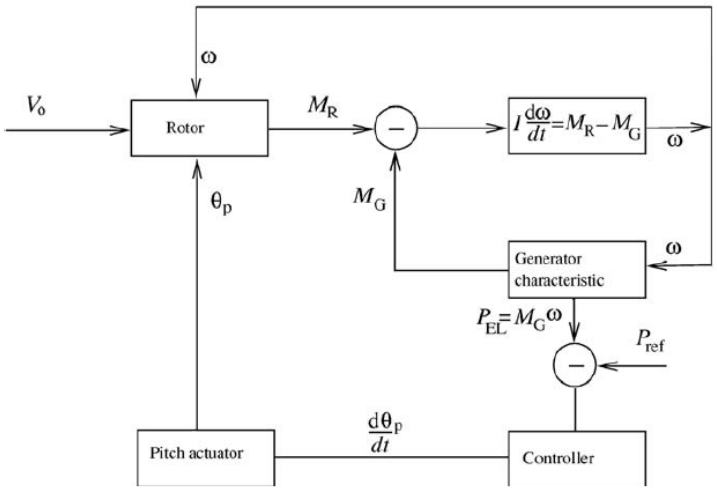

Figure 3: Active power control block diagram (extracted from [13])

3 Experimental Campaign

The experimental setup consisted of 2 wind turbine models, in the following named `G1`s, whose rotor diameter (D) is 1.1m and their hub height (HH) is 0.825m. They were separated $4D$ in the streamwise direction and with a lateral shift of half a diameter. The undisturbed wind speed was measured by means of a Pitot tube, placed at hub height in front of the upstream model.

Each `G1` is equipped with a three-blades rotor whose rated rotating speed is 850 . Each carbon-made blade, mounted on the hub with two bearings, houses, within its hollow root, a small brushed motor equipped with a gear-head and a built-in relative encoder. This system enables, together with a dedicated electronic control board housed in the hub spinner, the individual pitch angle variation of the blade. The combined inertia of the rotor, shaft and generator considered at the low-speed side is $I = 1.39 \times 10^{-2} kg.m^2$

The model is controlled by a *M1 Bachmann* hard-real-time module. Similarly to what is done on real wind turbines, the *M1* implementes collective or individual pitch-torque control laws, similar to the ones described in [40] and references therein. For the generator torque controller (see equation 8), $K = 3.66 \times 10^{-6} \frac{N.m.s^2}{rad^2}$. A more detailed description of the `G1` and the wind tunnel can be found in [27]

4 Simulations setup and results

In this Section the numerical setup of the simulations and their results are presented. First a comparison of one simulation with the experimental data is done, and secondly we analyze simulations performed with 5 different ABL profiles as inlets.

4.1 Numerical setup

The size of the computational domain is 27.50m in the streamwise direction, 5.50m in the spanwise direction and 4.50m in the vertical direction. It is uniformly divided in the streamwise and spanwise direction with 384 and 96 grid cells respectively, while a stretched grid is used in the vertical direction with 80 grid cells, covering one vertical rotor diameter with 30 grid cells. In [27] two additional spatial resolutions have been tested for a stand-alone model wind turbine with the same numerical setup, obtaining an acceptable agreement with experimental data using the spatial resolution considered in the current paper. The Crank-Nicolson scheme is used to advance in time with a step of 0.005 seconds. 5000 time steps are simulated, which means 25 seconds of the `G1s` oparation and accounts for approximately 300 turns of their rotor. The scale dependent dynamic Smagorinsky model with local averaging scheme is used to compute the sub-grid scale stress, as in previous studies [35, 37] better results were obtained with this sub-grid scale model. The model wind turbine is placed $2D$ from the inlet. For further details on the numerical setup, please see [27].

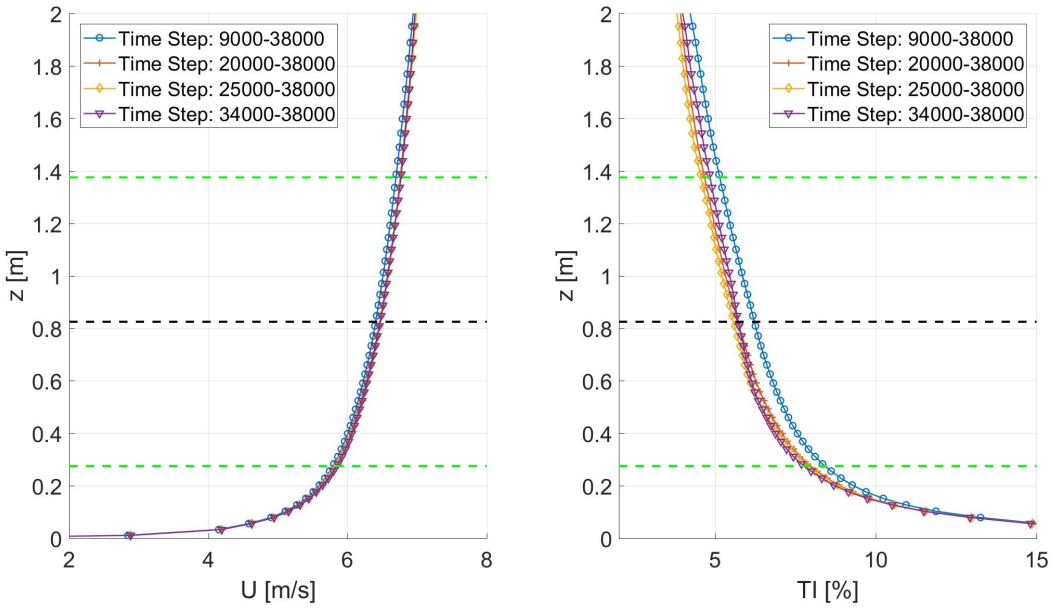

Figure 4: Span-wise averaged vertical profiles, at different time steps. Left: stream-wise velocity component (U), right: stream-wise turbulence intensity (TI). The black and green dotted lines represents the WT hub height and blades tip, respectively

The 2 wind turbine arrangement described in Section 3 was simulated subject to different ABL inflow conditions. These were obtained from precursor simulations, taking into account the same numerical setup described previously, but without wind turbines and applying a periodic boundary condition in the west and east boundaries and a constant pressure gradient as forcing term. After statistical convergence is reached, the velocity flow is considered at the inlet of the simulation with HAWTs. Figure 4 shows span-wise averages of the down-stream velocity component (U) and of the turbulent intensity (TI) vertical profiles, between different time steps of one precursor simulation. The turbulent intensity is calculated considering the stream-wise velocity component, according to equation 10, where σ(U) is the standard deviation of U.

$$TI = \sigma(U)/\overline{U} \tag{10}$$

The ABL profile shown in Figure 4 has a mean streamwise velocity component of 6.4m/s at hub height, a streamwise turbulence intensity of approx. 5.9% and is characterized by a power law with shear exponent of 0.1. Notice that after 20.000 time steps, the variation of U and TI vertical profiles is negligible, and thus convergence is achived. At the experimental campaign U was 6.1m/s and TI = 3.7%, obtained from the Pitot tube measurements, which accounts for 5% difference in velocity at hub-height with respect to the simulation.

4.2 Results

In this Section the results of the simulations are presented: first, the data obtained from one simulation is compared with data from the experimental campaign described in 3, and secondly the influence of considering different wind flows at the inlet of the simulations is depicted.

To avoid the transient effect on the flow produced by the sudden inclusion of the turbines in the domain, the first 1000 time steps of the simulation, equivalent to 5 seconds, are discarded in the results shown and to calculate temporary averages of the `G1` signals. The considered signals are the downstream velocity component (U), the rotor angular speed, the blade-pitch-angle and the active power output, both aerodynamic and electric. A comparison of the temporal evolution of the signals between the experimental and numerical data of the first WT can be seen in Figure 5.

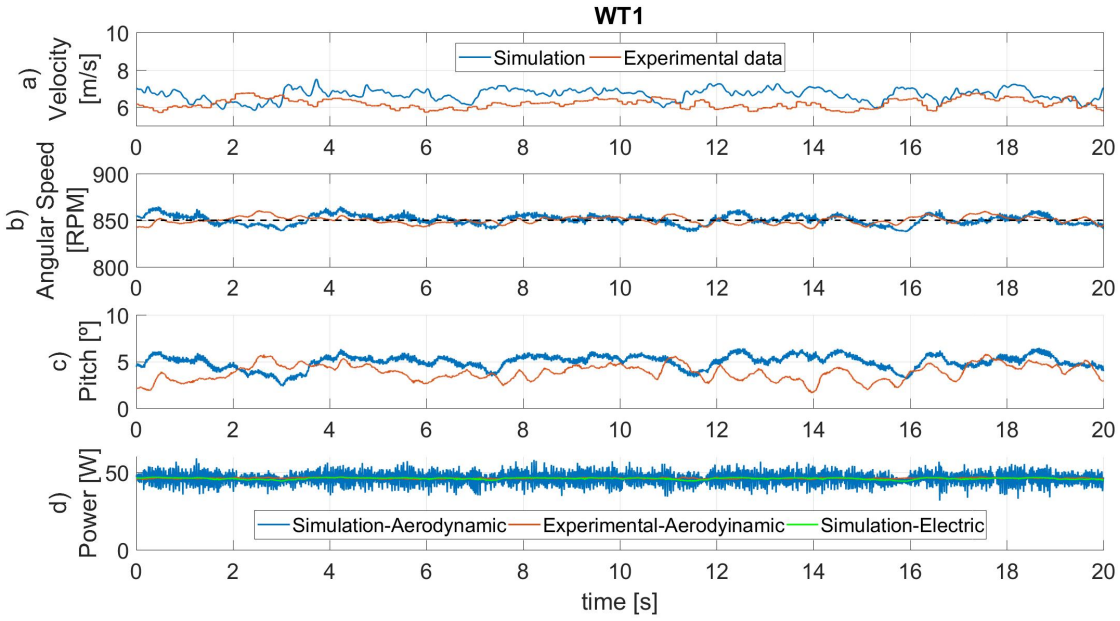

Figure 5: Temporal evolution of Wind Speed (top) Rotational Speed (middle-top), Pitch angle (middle-bottom) and Power production (bottom) of the first WT

Good agreement is found in the mean value of all the signals, with a slight overestimation of the pitch. The difference in wind velocity, being higher in the simulation, may explain this difference, as the aerodynamic torque is higher and thus a greater pitch angle is required to regulate the rotor speed. Also, larger fluctuations can be noticed when comparing the simulation aerodynamic power with the measured one. Although the higher TI at the inlet of the simulations may contribute to these difference, the reasons are not clear yet. On the other side, if the electric power output is considered, represented as the dotted green line and calculated as equation 7, the fluctuations are significantly reduced. It can be noticed that the angular speed signal fluctuates around the rated value, 850RPM, represented by the dotted black line.

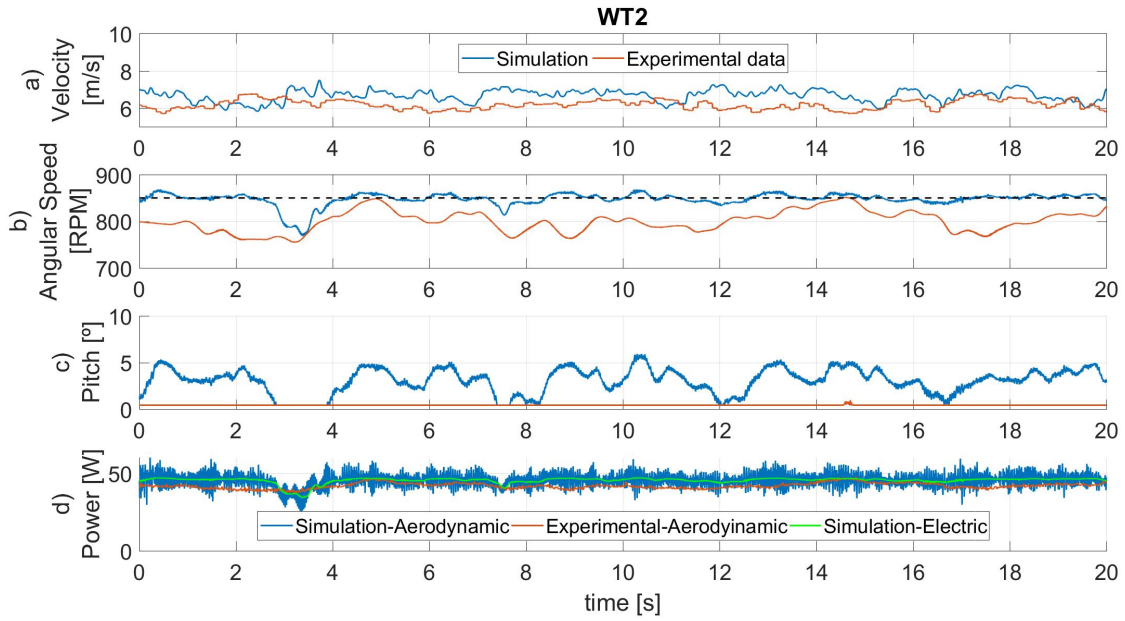

Figure 6: Temporal evolution of Wind Speed (top) Rotational Speed (middle-top), Pitch angle (middle-bottom) and Power production (bottom) of the second WT

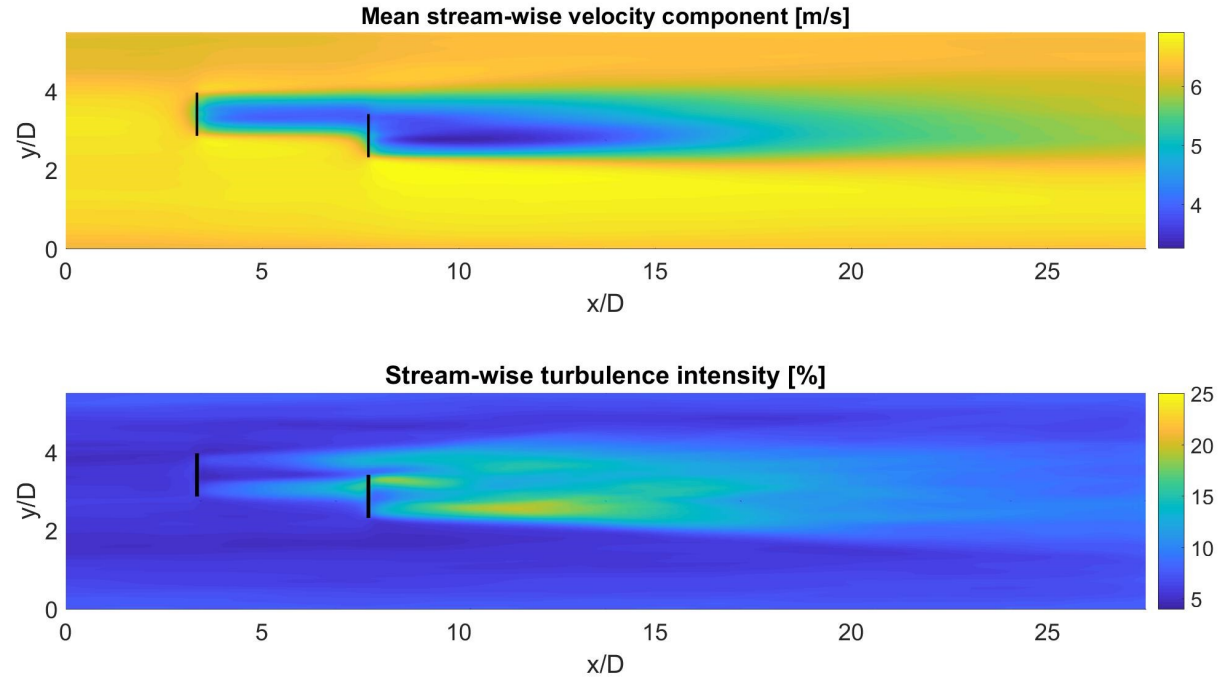

Figure 7: Mean stream-wise velocity component (top) and mean stream-wise turbulence intensity (bottom) on a horizontal plane at hub height. The wind turbines are represented by the black lines

On the other side, the second WT presents higher differences in all three signals, as it can be seen in Figure 6. Although no measurements of the velocity upstream of the second WT were taken in the experimental campaign, we suppose that the velocity deficit induced by the first WT may have been considerably lower

than the one obtained in the simulation. Again, the main reason for this could be the difference in velocity at the inlet between the simulation and the experimental data, which caused that in the experimental campaign the second G1 rarely reached its rated rotational speed, while in the simulation it does, and explains why the pitch-angle was kept constant at its minimum value and why the measured power is overestimated by 8%. Notice that the velocity signal in Figure 6 is the same as in Figure 5, and it corresponds to the Pitot tube measurement for the experimental, and to the span-wise average of the velocity at cells located in the inlet at hub height and upstream of the first WT, for the simulation data.

Figure 7 shows the mean stream-wise velocity component and turbulence intensity (TI) on a horizontal plane at hub height. That figure shows the wake deficit downstream the rotor, characterized by a large velocity deficit in the wake center and extending beyond $10D$ downstream, and an increase in TI, particularly at the blade tips.

To test the power controller at wind velocities higher than the rated one, the 2 wind turbines arrangement was simulated subject to four other ABL inflow conditions. Figure 8 depicts the mean stream-wise velocity component (U) and TI, at the inlet and averaged along the span-wise direction. Inlet 2 corresponds to the simulation presented previously in this section. Table 1 depicts U and TI at hub height (HH) for each simulation

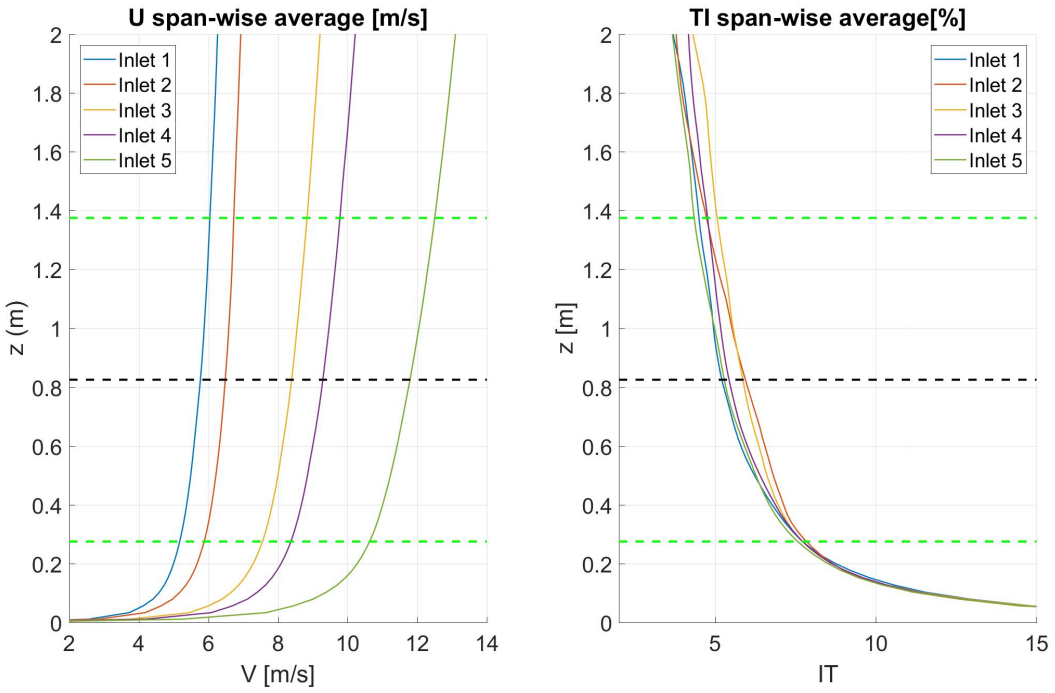

Figure 8: Span-wise averaged vertical profiles of the five simulation's inlets. Left: stream-wise velocity component (U), right: stream-wise turbulence intensity (TI). The black and green dotted lines represents the G1s hub height and blades tip, respectively

The temporal mean values of power, power coefficient (CP) and pitch angles were computed and plotted against the mean stream-wise velocity component at hub height, for both wind turbines. This is shown in Figure 9, where the experimental data are included considering the wind velocity measured by the Pitot.

The mean power coefficient is calculated according to equation 11. In this equation, U represents the average of the velocity in cells at the inlet, at hub height and up-stream of the first WT. The reason to consider only these cells and not the whole span-wise direction, is that as it can be noticed on Figure 7, the velocity at the inlet is not uniform along span-wise variation, with a difference of 10% between the maximum and minimum value at hub height. Particularly, in the cells of the domain located up-stream of the first WT there is a zone of higher velocities. The same was noticed at the experimental campaign, where a difference in velocity of 6% along the span-wise section was reported in [41]. In equation 11, P accounts for the electric

Table 1: U and TI of inlets at hub height.

Profile	$U_{HH}[m/s]$	$TI_{HH}[\%]$
Inlet 1	5.8	5.2
Inlet 2	6.5	5.9
Inlet 3	8.4	5.8
Inlet 4	9.3	5.4
Inlet 5	11.8	5.3

power, ρ the air density, $1.2kg/m^3$ and A the area swept by the rotor, equivalent to $D^2\pi/4$. Notice that the same wind velocity is considered to calculate the CP of both wind turbines, although the second `G1` is located in the wake of the first one, and thus the velocity is significantly lower. This difference in velocity leads to a CP lower to what is expected for the second turbine, which is operating below rated wind speed.

$$CP = \langle \frac{P}{0.5U^3\rho A} \rangle = \langle \frac{8P}{U^3\rho D^2\pi} \rangle \tag{11}$$

Good agreement is found in the the experimental and simulated CP of the first `G1`. For the second wind turbine, the interpolated value of the mean power coefficient is 0.284, which has a difference of 7% compared to the 0.304 of the experimental data. Again, the main reason for this difference may be caused by the sensibility of the CP to the reference velocity (U), which has significant span-wise variation both in the simulation and in the experiments.

In Figure 9 it can be observed that for velocities higher than the rated one, both `G1`s operate at rated power and the power coefficient decreases while the pitch angle increases, as it is expected for the operation of pitch-controlled wind turbines, according to [13]

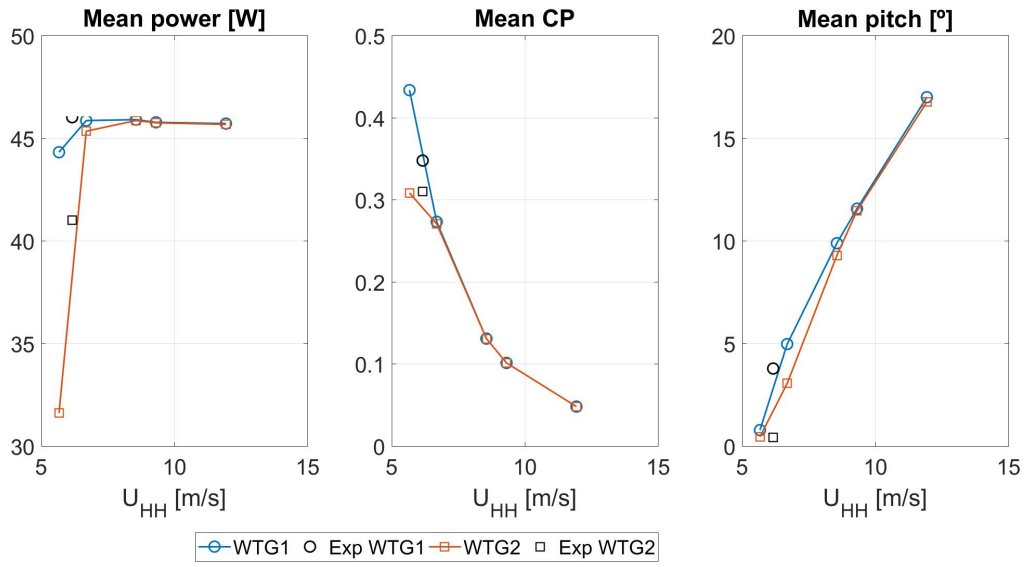

Figure 9: Mean power, CP and pitch vs mean stream-wise velocity at hub height

The temporal evolution of the variables of the first and second WT are depicted in Figures 10 and 11. Inlet 1 has a mean stream-wise velocity component at hub height of 5.8m/s, which is slightly lower than Inlet 2, and causes that the first WT occasionally does not reach its rated speed, and in those cases the pitch

is kept constant at its minimum value. For the second WT it is clear that it does not reach rated speed, and its operation resembles to what is observed in the experimental campaign (see Figure 6). For the rest of the simulations, with higher wind velocity at the inlet, both the rotor speed and the power output oscillates around the rated value, for both wind turbines, which proves that the power controller works correctly.

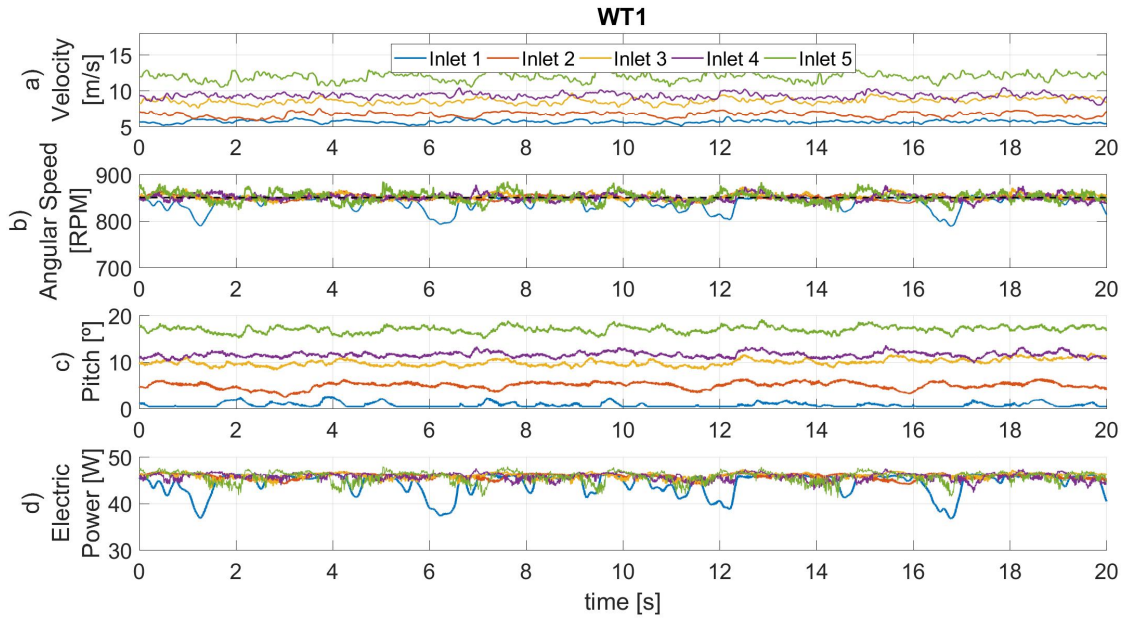

Figure 10: Temporal evolution of simulation signals of the first WT

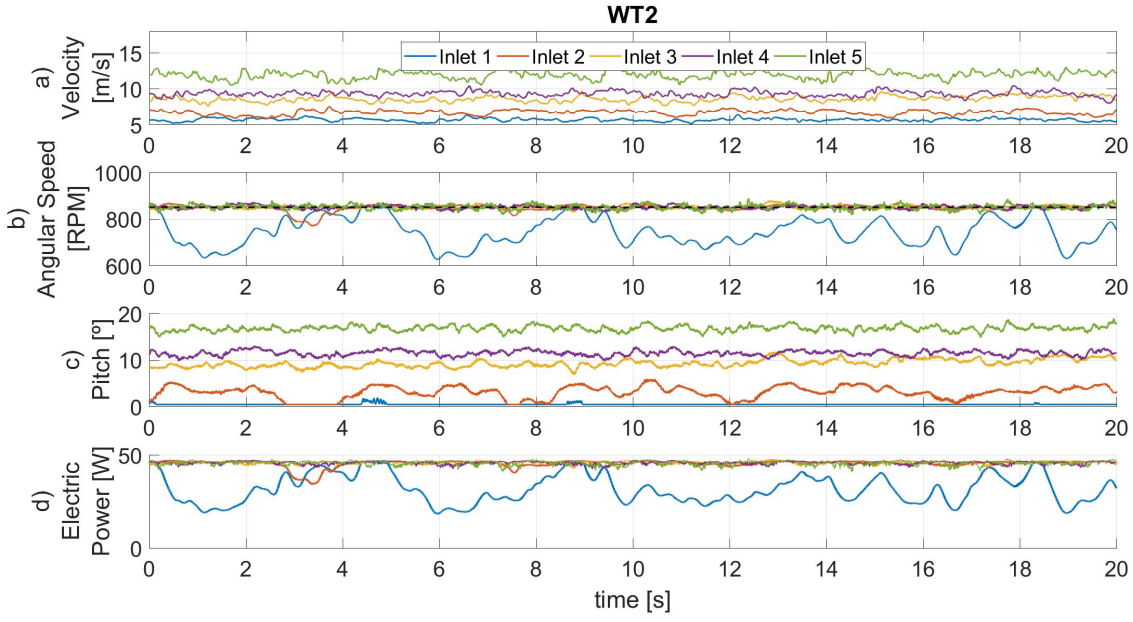

Figure 11: Temporal evolution of simulation signals of the second WT

5 Conclusion and Future Work

A Large Eddy Simulation framework with the Actuator Line Model to represent the wind turbine rotors has been used to simulate the operation of a two semi-aligned wind turbine arrangement, subject to five different ABL wind profiles with hub height velocities close or higher than the rated one. The results of the simulations were compared to an experimental campaign developed at Politecnico di Milano wind tunnel.

A closed-loop collective-pitch and a torque controller was implemented in the CFD code, as a series of subroutines. This allowed to simulate the whole range of operation of the wind turbines. In general, an acceptable agreement is obtained between the mean values of the experimental data and the numerical results, although significant differences in the amplitude of the signal of aerodynamic power were found when comparing the experimental and simulation data. The reasons for this are not clear yet, and we plan to keep investigating them.

Future research will focus on the use of this numerical framework to study wind farm control strategies, both for maximizing power production and for active power control. The use of GPU computing platform as considered in [42] is now being expanded to the full flow solver, using a dual CUDA / OpenCL sintaxis on top of the coarse MPI parallelization. This approach allows achieving speedups of up to 30x with respect to the CPU only solver and will be next extended to the wind turbine module routines.

References

[1] GWEC. Global Wind Report 2015 | Gwec. *Wind energy technology*, page 75, 2016.

[2] J N Sorensen and W Z Shen. Numerical Modeling of Wind Turbine Wakes. *Journal of Fluids Engineering*, 124(2):393, 2002.

[3] F Porté-Agel, H Lu, and YT Wu. A large-eddy simulation framework for wind energy applications. *Fifth International Symposium on ...*, 2010.

[4] M Churchfield, S Lee, P Moriarty, L Martinez, S Leonardi, Ganesh Vijayakumar, and James Brasseur. A Large-Eddy Simulations of Wind-Plant Aerodynamics. *50th AIAA Aerospace Sciences Meeting including the New Horizons Forum and Aerospace Exposition*, 2012.

[5] P K Jha, M J Churchfield, P J Moriarty, and Sven Schmitz. Accuracy of state-of-the-art actuator-line modeling for wind turbine wakes. *AIAA Paper*, (2013-0608), 2013.

[6] N Troldborg, J Nørkær, and R Flemming. *Actuator Line Modeling of Wind Turbine Wakes by N Troldborg Dissertation submitted to the Technical University of Denmark in partial fulfillment of.* 2009.

[7] L A Mart\'\inez-Tossas, M J Churchfield, and S Leonardi. Large eddy simulations of the flow past wind turbines: actuator line and disk modeling. *Wind Energy*, 18(6):1047–1060, 2014.

[8] N Troldborg, F Zahle, P E Réthoré, and N N Sørensen. Comparison of wind turbine wake properties in non-sheared inflow predicted by different computational fluid dynamics rotor models. *Wind Energy*, 18(7):1239–1250, 2015.

[9] S Ivanell, R Mikkelsen, J N Sørensen, and D Henningson. Validation of methods using EllipSys3D. pages 183–221, 2008.

[10] R J A M Stevens, L A Mart\'\inez-Tossas, and C Meneveau. Comparison of wind farm large eddy simulations using actuator disk and actuator line models with wind tunnel experiments. *Renewable Energy*, 116:470–478, 2018.

[11] J. M. Jonkman and M. L. Jr. Buhl. FAST User's Guide - Updated August 2005. (October), 2005.

[12] Stig Øye. Dynamisk, aeroelastisk beregning af vindmøllevinger. Technical report, DTU, 1983.

[13] K S Hansen, R J Barthelmie, L E Jensen, and A Sommer. The impact of turbulence intensity and atmospheric stability on power deficits due to wind turbine wakes at Horns Rev wind farm. *Wind Energy*.

[14] T Burton, N Jenkins, D Sharpe, and E Bossanyi. *Wind Energy Handbook*. 2011.

[15] R Storey and SE Norris. Large Eddy Simulation of Dynamically Controlled Wind Turbines. *Ewea Offshore 2011*, (January):1–10, 2011.

[16] P Fleming, S Lee, M Churchfield, A Scholbrock, J Michalakes, K Johnson, and P Moriarty. The SOWFA Super-Controller : A High-Fidelity Tool for Evaluating Wind Plant Control Approaches. *European Wind Energy Association 2013*, (January), 2013.

[17] R Mikkelsen, Jens N. Sørensen, Stig Øye, and N Troldborg. Analysis of power enhancement for a row of wind turbines using the actuator line technique. *Journal of Physics: Conference Series*, 75(1), 2007.
[18] Xiaolei Yang, Jennifer Annoni, Pete Seiler, and Fotis Sotiropoulos. Modeling the effect of control on the wake of a utility-scale turbine via large-eddy simulation. In *Journal of Physics: Conference Series*, volume 524, page 12180. IOP Publishing, 2014.
[19] Y Wu and F Porté-Agel. Modeling turbine wakes and power losses within a wind farm using LES: An application to the Horns Rev offshore wind farm. *Renewable Energy*, 75:945–955, 2015.
[20] M Mendina, M Draper, A P Kelm Soares, G Narancio, and G Usera. A general purpose parallel block structured open source incompressible flow solver. *Cluster Computing*, 17(2):231–241, 2014.
[21] G Usera, A Vernet, and J A Ferré. A Parallel Block-Structured Finite Volume Method for Flows in Complex Geometry with Sliding Interfaces. *Flow, Turbulence and Combustion*, 81(3):471, 2008.
[22] J Jonkman, S Butterfield, W Musial, and G Scott. Definition of a 5-MW Reference Wind Turbine for Offshore System Development. (February), 2009.
[23] C L Bottasso, F Campagnolo, and V Petrović. Wind tunnel testing of scaled wind turbine models: Beyond aerodynamics. *Journal of Wind Engineering and Industrial Aerodynamics*, 127(Supplement C):11–28, 2014.
[24] F Campagnolo, V Petrović, J Schreiber, E M Nanos, A Croce, and C L Bottasso. Wind tunnel testing of a closed-loop wake deflection controller for wind farm power maximization. *Journal of Physics: Conference Series*, 753:32006, sep 2016.
[25] F Campagnolo, V Petrović, C L Bottasso, and A Croce. Wind tunnel testing of wake control strategies. In *2016 American Control Conference (ACC)*, pages 513–518, 2016.
[26] F Campagnolo, V Petrović, E Nanos, C Tan, C L Bottasso, I Paek, and H Kim K Kim. Wind tunnel testing of power maximization control strategies applied to a multi-turbine floating wind power platform. In *Proceedings of the International Offshore and Polar Engineering Conference*, 2016.
[27] M Draper, A Guggeri, M Mendina, G Usera, and F Campagnolo. A Large Eddy Simulation model for the study of wind turbine interactions and its application. In *10th International Conference on Compuational Fluid Dynamimcs , Barcelona, Accepted for presentation*, 2018.
[28] J H Ferziger and M Peric. *Computational Methods for Fluid Dynamics*. Springer-Verlag Berlin Heidelberg, 3 edition, 2002.
[29] J Smagorinsky. General circulation experiments with the primitive equations: I. The basic experiment. *Monthly weather review*, 91(3):99–164, 1963.
[30] P J Mason and D J Thomson. Stochastic backscatter in large-eddy simulations of boundary layers. *Journal of Fluid Mechanics*, 242:51–78, 1992.
[31] M Germano, U Piomelli, P Moin, and W H Cabot. A dynamic subgrid-scale eddy viscosity model. *Physics of Fluids A: Fluid Dynamics*, 3(7):1760–1765, 1991.
[32] Y Zang, R L Street, and J R Koseff. A dynamic mixed subgrid-scale model and its application to turbulent recirculating flows. *Physics of Fluids A: Fluid Dynamics*, 5(12):3186–3196, 1993.
[33] F Porté-Agel, C Meneveau, and M B Parlange. A scale-dependent dynamic model for large-eddy simulation: application to a neutral atmospheric boundary layer. *Journal of Fluid Mechanics*, 415:261–284, 2000.
[34] M Draper. *Simulación del campo de vientos y de la interacción entre aerogeneradores*. PhD thesis, 2015.
[35] M Draper and G Usera. Evaluation of the Actuator Line Model with coarse resolutions. *Journal of Physics: Conference Series*, 625(1):12021, 2015.
[36] M Draper, A Guggeri, and G Usera. Validation of the Actuator Line Model with coarse resolution in atmospheric sheared and turbulent inflow. *Journal of Physics: Conference Series*, 753(8), 2016.
[37] M Draper, A Guggeri, and G Usera. Modelling one row of Horns Rev wind farm with the Actuator Line Model with coarse resolution. *Journal of Physics: Conference Series*, 753(8), 2016.
[38] M Draper, A Guggeri, and G Usera. Modelling one row of Horns Rev wind farm with the Actuator Line Model with coarse resolution. *Journal of Physics: Conference Series*, 753:82028, sep 2016.
[39] A Guggeri, M Draper, and G Usera. Simulation of a 7.7 MW onshore wind farm with the Actuator Line Model. *Journal of Physics: Conference Series*, 854(1), 2017.
[40] E A Bossanyi. The Design of closed loop controllers for wind turbines. *Wind Energy*, 3(3):149–163, 2000.
[41] J Wang, S Foley, E M Nanos, T Y, F Campagnolo, C L Bottasso, A Zanotti, and A Croce. Numerical

and Experimental Study of Wake Redirection Techniques in a Boundary Layer Wind Tunnel. *Journal of Physics: Conference Series*, 854:12048, may 2017.

[42] P Igounet, P Alfaro, G Usera, and P Ezzatti. Towards a finite volume model on a many-core platform. *International Journal of High Performance Systems Architecture 12*, 4(2):78–88, 2012.